Inorganic Chemistry
Article
pubs.acs.org/IC
Terms of Use CC-BY

Exchange Interactions at the Origin of Slow Relaxation of the Magnetization in {TbCu$_3$} and {DyCu$_3$} Single-Molecule Magnets

Fraser J. Kettles,[†] Victoria A. Milway,[†] Floriana Tuna,[‡] Rafael Valiente,[§] Lynne H. Thomas,[⊥] Wolfgang Wernsdorfer,[∥] Stefan T. Ochsenbein,*[,#] and Mark Murrie*[,†]

[†]WestCHEM, School of Chemistry, University of Glasgow, Glasgow G12 8QQ, U.K.

[‡]EPSRC National UK EPR Facility, School of Chemistry and Photon Science Institute, The University of Manchester, Manchester M13 9PL, U.K.

[§]MALTA-Consolider Team, Dpt. Física Aplicada, Facultad de Ciencias, Universidad de Cantabria, Av los Castros s/n, 39005 Santander, Spain

[⊥]Department of Chemistry, University of Bath, Claverton Down, Bath BA2 7AY, U.K.

[∥]Institut Néel, CNRS, Nanosciences Department, BP 166, 25 rue des Martyrs, 38042 Grenoble Cedex 9, France

[#]Laboratory for Neutron Scattering and Imaging, Paul Scherrer Institut, CH-5232 Villigen, Switzerland

Supporting Information

ABSTRACT: New {TbCu$_3$} and {DyCu$_3$} single-molecule magnets (SMMs) containing a low-symmetry Ln^{III} center (shape measurements relative to a trigonal dodecahedron and biaugmented trigonal prism are 2.2−2.3) surrounded by three Cu^{II} metalloligands are reported. SMM behavior is confirmed by frequency-dependent out-of-phase ac susceptibility signals and single-crystal temperature and sweep rate dependent hysteresis loops. The ferromagnetic exchange interactions between the central Ln^{III} ion and the three Cu^{II} ions could be accurately measured by inelastic neutron scattering (INS) spectroscopy and modeled effectively. The excitations observed by INS correspond to flipping of Cu^{II} spins and appear at energies similar to the thermodynamic barrier for relaxation of the magnetization, ∼15−20 K, and are thus at the origin of the SMM behavior. The magnetic quantum number M_{tot} of the cluster ground state of {DyCu$_3$} is an integer, whereas it is a half-integer for {TbCu$_3$}, which explains their vastly different quantum tunneling of the magnetization behavior despite similar energy barriers.

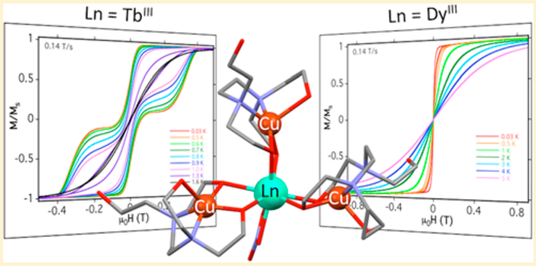

INTRODUCTION

Single-molecule magnets (SMMs) display slow relaxation of the magnetization of purely molecular origin and have remained a hot topic because of their fundamental physics and potential applications.[1] The majority of SMMs have been molecular 3d transition-metal complexes,[2] but in recent years, lanthanide-containing molecules have gained prominence.[3] 3d−4f complexes are also good candidates for SMMs: very large single-ion magnetic anisotropies have been observed for Tb^{III} and Dy^{III},[4] and ferromagnetic coupling is commonly observed between Cu^{II} and ions such as Gd^{III}, Tb^{III}, and Dy^{III}.[5] In comparison to polynuclear Ln^{III}-based SMMs,[3,6] there are relatively few Tb^{III}Cu^{II} SMMs, these using Schiff base or macrocyclic ligands, and even fewer Dy^{III}Cu^{II} SMMs.[7] Furthermore, the origin of slow relaxation of the magnetization in 3d−4f SMMs needs more detailed investigation. The main interactions governing magnetic properties in 3d−4f SMMs are the crystal-field interactions of the lanthanide ions and the exchange interactions between lanthanide ions and transition-metal ions. We report a new family of {LnCu$_3$} complexes (Ln = Gd^{III}, Tb^{III}, Dy^{III}), of which the Tb^{III} and Dy^{III} analogues show slow relaxation of magnetization. We have determined the exchange interactions in {TbCu$_3$} and {DyCu$_3$} with inelastic neutron scattering (INS) spectroscopy, a powerful technique often used to measure crystal-field and exchange splittings in molecular clusters,[8] with pioneering work on lanthanide-containing clusters done by Furrer, Güdel, and co-workers.[9] Despite its obvious potential, especially for Ln clusters, very few Ln-containing SMMs have thus far been studied with INS spectroscopy.[10] We found that the fundamental INS excitations correspond to Cu^{II} spin flips, which have energies similar to the barriers for magnetization reversal that we determined using ac magnetic susceptibility measurements. These findings indicate the importance of these spin flips for the magnetic relaxation and therefore of the 3d−4f exchange interactions. Furthermore, the nature of the ground state (M_{tot} = integer or half-integer) determines the effectiveness of quantum tunneling of the magnetization (QTM).

EXPERIMENTAL SECTION

Syntheses. *[Cu$_2$(H$_3$edte)$_2$][NO$_3$]$_2$.* To a solution of 2,2′,2″,2‴-(ethane-1,2-diyldinitrilo)tetraethanol (H$_4$edte; 12.68 g, 53.68 mmol) in

Received: April 16, 2014
Published: August 7, 2014

dx.doi.org/10.1021/ic500885r | Inorg. Chem. 2014, 53, 8970−8978

100 mL of MeCN was slowly added a solution of $Cu(NO_3)_2·3H_2O$ (6.65 g, 27.52 mmol) in 100 mL of MeCN with vigorous stirring. The reaction mixture was stirred at room temperature overnight to yield a green precipitate, which was collected by filtration, washed with MeCN, and then air-dried. Yield: 95% based on Cu. Vapor diffusion of redissolved precipitate in MeOH with Et_2O produced blue-green plates suitable for X-ray diffraction. Anal. Calcd for $C_{20}H_{46}Cu_2N_6O_{14}$: C, 33.28; H, 6.42; N, 11.64. Found: C, 33.24; H, 6.47; N, 11.52. Selected IR peaks (cm^{-1}): 3468 (w), 3284 (br), 2955 (w), 2914 (w), 2881 (w), 2854 (w), 1753 (w), 1477 (w), 1452 (m), 1371 (s), 1311 (s), 1265 (m), 1209 (w), 1165 (w), 1143 (w), 1099 (m), 1064 (s), 1041 (s), 1028 (s), 1016 (s), 1004 (m), 991 (m), 974 (m), 922 (m), 902 (m), 883 (m), 868 (m), 825 (m), 792 (m), 759 (m), 723 (m), 640 (m).

$[GdCu_3(H_2edte)_3(NO_3)][NO_3]_2·0.5MeOH$ ({$GdCu_3$}). To a stirred solution of $[Cu_2(H_3edte)_2][NO_3]_2$ (0.4 g, 0.55 mmol) and NEt_3 (0.21 mL, 1.5 mmol) in MeOH (20 mL) was added $Gd(NO_3)_3·6H_2O$ (0.112 g, 0.25 mmol). The reaction mixture was stirred at room temperature overnight to yield a blue precipitate, which was collected by filtration, washed with EtOH, and then air-dried. Yield: 89%. Vapor diffusion of redissolved precipitate in MeOH with THF produced blue platelike needles suitable for X-ray diffraction. Anal. Calcd for $C_{30}H_{66}Cu_3GdN_9O_{21}$: C, 29.13; H, 5.38; N, 10.19. Found: C, 29.0; H, 5.41; N, 9.91. Selected IR peaks (cm^{-1}): 3200 (br), 2889 (w), 2835 (w), 2686 (w), 1465 (m), 1440 (m), 1383 (m), 1338 (m), 1301 (s), 1263 (m), 1170 (w), 1151 (w), 1139 (w), 1078 (s), 1057 (s), 1016 (s), 987 (m), 970 (m), 918 (m), 904 (m), 891 (m), 877 (m), 848 (w), 827 (m), 819 (w), 788 (w), 760 (w), 736 (m), 721 (m), 696 (w), 669 (w), 613 (m).

$[TbCu_3(H_2edte)_3(NO_3)][NO_3]_2·0.5MeOH$ ({$TbCu_3$}). To a stirred solution of $[Cu_2(H_3edte)_2][NO_3]_2$ (0.4 g, 0.55 mmol) and NEt_3 (0.21 mL, 1.5 mmol) in MeOH (20 mL) was added $Tb(NO_3)_3·5H_2O$ (0.108 g, 0.25 mmol). The reaction mixture was stirred at room temperature overnight to yield a blue precipitate, which was collected by filtration, washed with EtOH, and then air-dried. Yield: 88%. Vapor diffusion of redissolved precipitate in MeOH with THF produced blue platelike needles suitable for X-ray diffraction. Anal. Calcd for $C_{30}H_{66}Cu_3TbN_9O_{21}$: C, 29.09; H, 5.37; N, 10.18. Found: C, 29.04; H, 5.37; N, 9.94. Selected IR peaks (cm^{-1}): 3200 (br), 2928 (w), 2895 (w), 2864 (w), 2833 (w), 2789 (w), 2740 (w), 2681 (w), 2650 (w), 1465 (m), 1440 (m), 1383 (m), 1348 (m), 1338 (m), 1303 (s), 1263 (m), 1170 (w), 1151 (w), 1139 (w), 1078 (s), 1057 (s), 1016 (s), 987 (m), 970 (m), 916 (m), 904 (m), 891 (m), 875 (m), 844 (w), 827 (m), 819 (m), 788 (w), 758 (w), 736 (m), 725 (m), 677 (m), 657 (w), 613 (w).

$[DyCu_3(H_2edte)_3(NO_3)][NO_3]_2·0.5MeOH$ ({$DyCu_3$}). To a stirred solution of $[Cu_2(H_3edte)_2][NO_3]_2$ (0.4 g, 0.55 mmol) and NEt_3 (0.21 mL, 1.5 mmol) in MeOH (20 mL) was added $Dy(NO_3)_3·5H_2O$ (0.109 g, 0.25 mmol). The reaction mixture was stirred at room temperature overnight to yield a blue precipitate, which was collected by filtration, washed with EtOH, and then air-dried. Yield: 76%. Vapor diffusion of redissolved precipitate in MeOH with THF produced blue platelike needles suitable for X-ray diffraction. Anal. Calcd for $C_{30}H_{66}Cu_3DyN_9O_{21}$: C, 29.01; H, 5.36; N, 10.15. Found: C, 28.66; H, 5.49; N, 9.80. Selected IR peaks (cm^{-1}): 3200 (br), 2974 (w), 2947 (w), 2897 (w), 2843 (w), 2694 (w), 1747 (w), 1610 (w), 1465 (m), 1435 (m), 1413 (m), 1383 (m), 1354 (m), 1313 (s), 1259 (m), 1234 (m), 1170 (w), 1149 (w), 1107 (w), 1078 (s), 1057 (s), 1033 (s), 1014 (s), 985 (m), 922 (m), 908 (m), 893 (m), 883 (m), 869 (m), 844 (w), 825 (m), 817 (m), 756 (m), 725 (m), 675 (m), 646 (m), 605 (w).

Single-Crystal X-ray Diffraction. Data were collected at 100 K on a Bruker Nonius Kappa CCD diffractometer, equipped with a graphite-monochromated Mo Kα source (λ = 0.71073 Å). Absorption corrections were applied using a multiscan method (SADABS). The structure was solved and refined using Shelxs-97 and Shelxl-2013, respectively.[11] All non-H atoms were refined with anisotropic displacement parameters, with the exception of those involved in disorder.

In the main cluster of {$GdCu_3$}, one of the H_2edte^{2-} ligands shows positional disorder; C20 is disordered over two positions (C20A and C20B, 55:45) and the atoms C13, C14, N4, C15, C16, O8, C17, and C18 are also disordered over two positions (labeled A and B, 65:35). These occupancies were freely refined and then were fixed for the final refinement cycles. These atoms could only be modeled with isotropic thermal parameters and pairs C13A and C13B, C14A and C14B, C17A and C17B, C18A and C18B, and O8A and O8B were constrained to take the same isotropic thermal parameter because of the close proximity of the two positions. The bond length between O8B and C16B was also constrained to ensure it took a standard bond length (1.4 Å).

In the main cluster of {$TbCu_3$} and {$DyCu_3$}, one of the H_2edte^{2-} ligands shows positional disorder; C6 is disordered over two positions (C6A, C6B, 70:30 or 55:45) and C9, C10, and O4 are also disordered over two positions (labeled A and B, 75:25 or 70:30). Atoms C1, C2, N1, C7, and C8 show elongated thermal parameters, but attempts to split these atoms to take two positions resulted in an implausible model. Again the relative occupancies were freely refined, and these were then fixed at their converged values. In {$TbCu_3$}, the atom pairs C9A and C9B, C10A and C10B, and O4A and O4B were constrained to have equal isotropic thermal parameters due to the close proximity of their positions in space. The C9B−C10B and C10B−O4B bond distances were also constrained to take standard values.

In all three {$LnCu_3$} compounds, the nitrate counterion molecule N200, O200, O201, and O202 is disordered over an inversion center; N200 and O200 sit directly on the inversion center and so were refined with 50% occupancy and constrained to take the same position and isotropic thermal parameter. Anisotropic refinement of this moiety resulted in unreasonable thermal parameters, probably due to small shifts in the positions for the two conformations that the molecules can adopt. It was not possible to resolve these two positions, and so the model was kept with isotropic thermal parameters. Consequently, there is some significant residual electron density in this region which remains unmodeled. A second nitrate counterion N100, O100, O101, and O102 is also disordered over an inversion center, but this time it does not sit directly on the inversion center and it is 50:50 disordered with a solvent methanol molecule C300 and O300. These were therefore refined with only isotropic thermal parameters in {$GdCu_3$} and {$DyCu_3$} but all except N200 and N300 could be refined anisotropically.

H atoms were placed on calculated positions and modeled as refining on the atoms to which they are bonded with the exception of those on coordinated O atoms of the H_2edte^{2-} ligands, which were identified in a Fourier difference map but constrained to take O−H distances of 0.82 Å and thermal parameters 1.2 times that of the atom to which they were bonded.

Other Physical Methods. Infrared (IR) spectra were recorded on a Shimadzu FTIR-8400S Fourier transform infrared spectrophotometer in the 4000−600 cm^{-1} range. Elemental analyses (C, H, and N) were performed in-house in the School of Chemistry at the University of Glasgow. Variable-temperature direct current (dc) and alternating current (ac) magnetic susceptibility data were collected on a Quantum Design MPMS-XL SQUID magnetometer equipped with a 7 T magnet and operating in the 1.8−300 K range. Powder samples were embedded in eicosane, to prevent torquing. Magnetic data have been corrected for diamagnetism (Pascal's constants and corrections for the sample holder). Ultralow-temperature (<1.8 K) hysteresis studies and dc relaxation measurements were performed on a single crystal using an array of micro-SQUIDS (the field is oriented along the easy axis, which is found in situ by changing the field orientation with three coils).[12] For the INS experiments, the samples were sealed under helium in a hollow aluminum cylinder ({$TbCu_3$}, outer diameter 12 mm, inner diameter 9 mm; {$DyCu_3$}, outer diameter 12 mm, inner diameter 10 mm). Initial neutron wavelengths (energies) of 4.3 Å (35.6 cm^{-1}) and 5.5 Å (21.8 cm^{-1}) were selected with the (002) reflection of the pyrolytic graphite monochromator. The spectra were corrected for the contributions of the sample environment and the sample holder by measuring an empty aluminum cell, while the detector efficiency was assessed using a vanadium sample. Data reduction was performed with DAVE.[13]

■ RESULTS AND DISCUSSION

Synthesis and Structure. To synthesize these new $Ln^{III}Cu^{II}$ complexes, we have developed our step-by-step approach, previously used to synthesize {$Mn_{18}Cu_6$} heterometallic

Table 1. Crystal Data and Structure Refinement Parameters

	$[Cu_2(H_3edte)_2][NO_3]_2$	$\{GdCu_3\}$	$\{TbCu_3\}$	$\{DyCu_3\}$
formula	$C_{20}H_{46}Cu_2N_6O_{14}$	$C_{30.5}H_{68}Cu_3GdN_9O_{21.5}$	$C_{30.5}H_{68}Cu_3TbN_9O_{21.5}$	$C_{30.5}H_{68}Cu_3DyN_9O_{21.5}$
M_r	721.71	1252.81	1254.48	1258.06
space group	$P2_1/c$	$P\bar{1}$	$P\bar{1}$	$P\bar{1}$
T, K	100	100	100	100
a, Å	8.9168(2)	8.9333(2)	8.9334(2)	8.9331(3)
b, Å	16.6076(3)	15.9959(4)	16.0024(4)	15.9760(6)
c, Å	9.7099(2)	16.2969(3)	16.3048(4)	16.3223(6)
α, deg	90	79.3690(10)	78.9190(10)	79.003(2)
β, deg	96.8680(10)	86.2750(10)	86.4920(10)	86.363(2)
γ, deg	90	82.5130(10)	82.839(2)	82.688(2)
V, Å^3	1427.59(5)	2267.28(9)	2267.91(10)	2266.24(14)
Z	2	2	2	2
ρ_{calcd}, g cm^{-3}	1.679	1.835	1.837	1.844
μ, mm^{-1}	1.57	2.92	3.02	3.11
$F(000)$	756	1274	1276	1278
no. of rflns collected	26980	50061	79068	49900
no. of indep rflns	2622	8033	8346	8527
obsd F_o ($>2\sigma(F)$)	2489	7419	6722	7187
R_{int}	0.03	0.0328	0.0874	0.0531
R1 (obsd)	0.0191	0.0398	0.0364	0.0395
wR2 (all)	0.0513	0.0903	0.0797	0.1005
GOF	1.059	1.164	1.05	1.066

complexes,[14] here using a similar ligand[15] to preform a Cu^{II} starting material, $[Cu_2(H_3edte)_2][NO_3]_2$ (H_4edte =2,2′,2″,2‴-(ethane-1,2-diyldinitrilo)tetraethanol). This dimeric Cu^{II} precursor can be prepared in 95% yield (see the Experimental Section and the Supporting Information), where the dicationic complex is structurally similar to that found in the previously reported compound $[Cu_2(H_3edte)_2][ClO_4]_2$.[16] Subsequent reaction of $[Cu_2(H_3edte)_2][NO_3]_2$ with $Ln(NO_3)_3{\cdot}xH_2O$ in MeOH in the presence of NEt_3 yields $[LnCu_3(H_2edte)_3(NO_3)][NO_3]_2{\cdot}0.5MeOH$ (Ln = Gd^{III}, Tb^{III}, Dy^{III}) in >70% yield (Table 1).

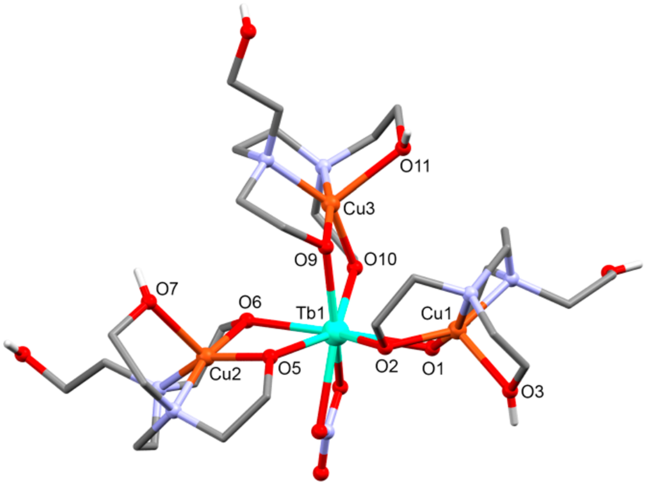

Figure 1. Structure of $[TbCu_3(H_2edte)_3(NO_3)]^{2+}$. Atom colors: Tb, cyan; Cu, orange; N, blue; O, red; C, gray. All hydrogen atoms except ligand OH groups are omitted for clarity.

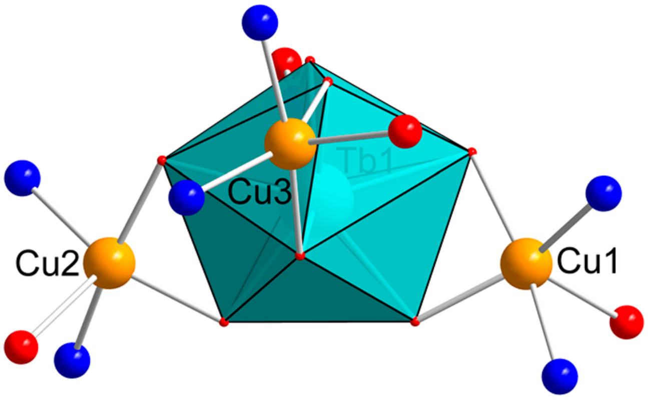

Figure 2. Core of $\{TbCu_3\}$, highlighting the distorted environment at Tb^{III}. Atom colors: Tb, cyan; Cu, orange; N, blue; O, red.

The $\{LnCu_3\}$ complexes consist of a central eight-coordinate Ln^{III} ion surrounded by three bidentate $\{CuH_2edte\}$ metalloligands and one bidentate nitrate ligand (Figure 1). The Ln^{III} ion is in a distorted environment (Figure 2) and shape measurements relative to a trigonal dodecahedron (D_{2d}) or biaugmented trigonal prism (C_{2v}) are the best match at 2.2−2.3 (see the Supporting Information, Table S1).[17] The next best match is for the Johnson-biaugmented trigonal prism (C_{2v}) or square antiprism (D_{4d}) at 2.9−3.3.[18−20] In $\{LnCu_3\}$, the steric properties of the $\{CuH_2edte\}$ metalloligands will play a key role in determining the shape of the Ln^{III} coordination sphere, encouraging further study into the utilization of flexible metalloligands to isolate rare or unusual Ln^{III} coordination geometries in 3d−4f complexes. Incorporation of a 3d metal ion such as Cu^{II} as the central ion of the metalloligand increases the flexibility further, due to its range of typical coordination environments from [4] to [4 + 2].[21] The Cu^{II} centers in $\{LnCu_3\}$ are in a distorted [4 + 1] environment $\{N_{2eq}O_{2eq}O_{ax}\}$, each encapsulated by a H_2edte^{2-} ligand. For each ligand, two arms are deprotonated and form alkoxide bridges between the Cu^{II} ion and the central Ln^{III} ion $\{Cu-\hat{O}-Ln$ = 96.71(13)−101.08(15)°$\}$. Two arms remain protonated: one fills the axial position (Cu−O = 2.203(4)−2.272(4) Å) and the other remains unbound, hydrogen bonded to adjacent $\{Cu_3Ln\}$ complexes and lattice nitrate anions.

Static Magnetic Properties. In the magnetic susceptibility data for $\{LnCu_3\}$ (Figure 3a), at low temperature the upturn in χT data is consistent with ferromagnetic exchange between Ln^{III} and Cu^{II}. Gd^{III} has a spin-only ground state ($S_{Gd} = 7/2$). Therefore, the χT data for $\{GdCu_3\}$ can be fit,[22] using a spin Hamiltonian with a single parameter $\mathcal{J}$ describing the exchange interaction between S_{Gd} and the three Cu^{II} spins ($s_i = 1/2$):

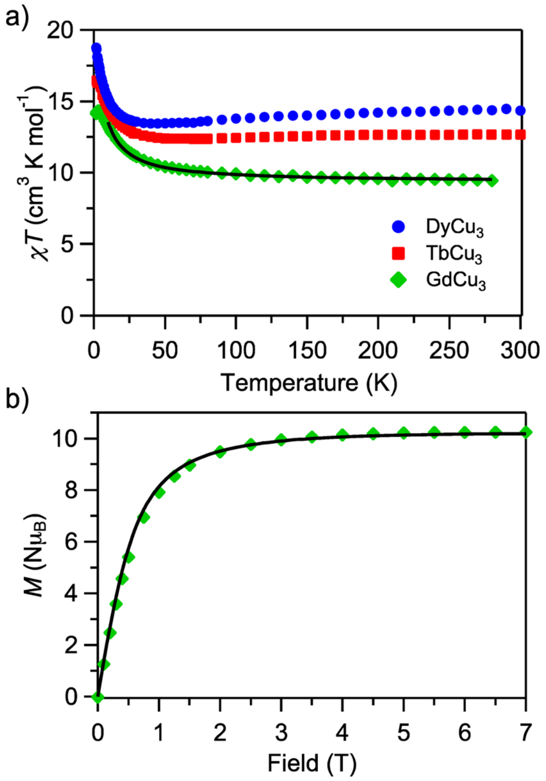

Figure 3. (a) Temperature dependence of χT for $\{LnCu_3\}$ from 300 to 1.8 K in a 1000 G field. (b) Magnetization versus field at 2 K for $\{GdCu_3\}$. The solid lines in (a) and (b) correspond to fits of the data with the parameters given in the text.

$$\mathcal{H} = -\mathcal{J}\sum_{i=1}^{3}(\vec{S}_{Gd}\vec{s}_i) + g\mu_B\vec{H}\left(\vec{S}_{Gd} + \sum_{i=1}^{3}\vec{s}_i\right) \qquad (1)$$

The second term in eq 1 is the Zeeman interaction, with μ_B being the Bohr magneton and $H = 1000$ G the magnetic field. The best-fit result between 10 and 280 K yields the parameters $g = 2.04(3)$ and $\mathcal{J} = 2.9(3)$ cm^{-1}, consistent with an $S = 5$ ground state of $\{GdCu_3\}$ (the small decrease at low temperature may be due to antiferromagnetic intercluster interactions or a small zero-field splitting and was excluded from the fit). This g value seems quite reasonable, considering that Gd^{III} has $g_{7/2} = 2.0$ and the Cu^{II} ions are expected to have a g value slightly larger than 2, giving credibility to this fit. These parameters also model the low-temperature magnetization versus field data for $\{GdCu_3\}$ very well, as can be seen in Figure 3b. N.B.: throughout this paper we adopt the notation J for total angular momentum and $\mathcal{J}$ for the exchange interaction parameters.

For $\{TbCu_3\}$ and $\{DyCu_3\}$ the crystal-field splitting of their respective $^7F_6$ and $^6H_{15/2}$ ground states is as important for the magnetic properties as the exchange interactions with the Cu^{II} spins. The lanthanide ion in each complex is in a low-symmetry environment (Table S1, Supporting Information). Therefore, many crystal-field terms (e.g., in the form of extended Stevens operators $\sum_{k=2,4,6}\sum_{q=-k}^{k} B_k^q \hat{O}_k^q$) are allowed by symmetry and their parameters are not correlated. This large number of parameters makes it virtually impossible to unequivocally model the featureless high-temperature magnetic susceptibility. At low temperatures, the susceptibilities of $\{TbCu_3\}$ and $\{DyCu_3\}$ increase due to the ferromagnetic exchange interactions between the lanthanide ion and the Cu^{II} ions, which impedes the determination of the low-energy crystal-field states from the magnetic susceptibility.

The magnetization data of $\{TbCu_3\}$ at 2 and 4 K and of $\{DyCu_3\}$ at 2, 4, and 6 K in Figure 4 show a steep increase at low fields, but not complete saturation at high fields, even at 2 K. These observations are consistent with a strongly anisotropic, large angular momentum ground state. We can safely assume that the crystal-field splitting of the Tb^{III} and the Dy^{III} ions is larger than the thermal energy in the magnetization experiments (maximum 6 K: $E_{thermal} \approx 4.2$ cm^{-1}) and that we only need to concern ourselves with their ground state, characterized by $M_J = \langle JM_J|\hat{J}_z|JM_J\rangle/\hbar$ $(-J \leq M_J \leq +J)$. Assuming the crystal-field splitting to be "axial enough" for (near) degenerate $\pm M_J$ doublets, an effective model allows fitting the magnetization, where the Ln^{III} ground doublet is replaced by an effective spin $S' = 1/2$:

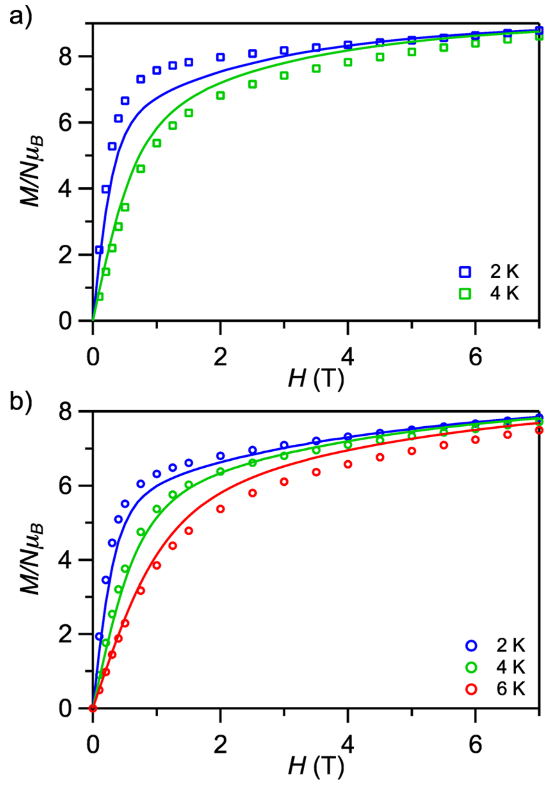

Figure 4. Magnetization curves of $\{TbCu_3\}$ at 2 and 4 K (a) and of $\{DyCu_3\}$ at 2, 4, and 6 K (b). The solid lines are fits based on the effective model (eq 2) with exchange parameters from INS, as described in the main text.

$$\mathcal{H} = -\sum_{i=1}^{3} \mathcal{J}_{ixy}(\hat{S}'_x\hat{s}_{ix} + \hat{S}'_y\hat{s}_{iy}) - \sum_{i=1}^{3} \mathcal{J}_{iz}\hat{S}'_z\hat{s}_{iz} + \mu_B\vec{H}\Big(g_{xy}(\hat{S}'_x + \hat{S}'_y) + g_z\hat{S}'_z + g_{Cu}\sum_{i=1}^{3}\vec{s}_i\Big) \qquad (2)$$

where $\mathcal{J}_{ixy}$ and $\mathcal{J}_{iz}$ are the effective parameters describing the anisotropic exchange interactions between S' and the Cu^{II} spins s_i = 1/2. The solid lines in Figure 4 are fits of the magnetization to this data, whereby the exchange parameters were taken from the INS measurements (vide infra). In such an effective model $g_z = g_J(2\alpha^2|M_J| + 2\beta^2|M'_J| + ...)$,[23] where the parameters α, β, ... describe the contribution of different M_J states to the wave function $|\Psi_0\rangle = \alpha|M_J\rangle + \beta|M'_J\rangle$ + ... of the Ln^{III} ground state and g_J values are the intrinsic Ln^{III} g factors for a given J multiplet.

For {TbCu$_3$}, the maximum g_z is therefore given as $g_z^{\max} = 2|M_J^{\max}|g_6 = 18$ ($g_6 = 3/2$, $|M_J^{\max}| = J = 6$), which was set as the upper limit for the fit. The following fit parameters were determined: $g_{xy} = 0(3)$, $g_z = 18(2)$, and $g_{Cu} = 2.4(3)$ with the exchange parameters $J_{xy} = 16.6$ cm^{-1} and $J_z = 26.7$ cm^{-1} (INS; vide infra). The magnetization of {DyCu$_3$} at 2, 4, and 6 K could be fit the same way, but with an upper limit of $g_z^{\max} = 2|M_J^{\max}|g_{15/2} = 20$ ($g_{15/2} = 4/3$, $|M_J^{\max}| = J = 15/2$). The best fit parameters are $g_{xy} = 0(1)$, $g_z = 16.9(6)$, and $g_{Cu} = 2.2(1)$ with the INS exchange parameters $\mathcal{J}_{xy} = 13.1$ cm^{-1} and $\mathcal{J}_z = 27.7$ cm^{-1} (vide infra).

For both {TbCu$_3$} and {DyCu$_3$} the fits yield reasonable values for the Cu^{II} g factor with the deviation between the two samples within the errors of the fit. The transverse g factor of the lanthanide ions g_{xy} is 0 in both cases, but with rather large error bars, indicating that its effect on the magnetization is marginal (see also contour plots of square of differences vs g_z and g_{xy} in the Supporting Information). From the values of g_z we can estimate the main M_J contribution to the lowest doublet of the crystal-field split states. In {TbCu$_3$} the maximum $g_z = 18(2)$ is found in the fit, which yields $M_J = \pm 6$ as the main contribution to the ground doublet wave function. For {DyCu$_3$}, $g_z = 16.9(6)$, which is quite close to the value 52/3 expected for $M_J = \pm 13/2$, and we thus conclude that the ground doublet of Dy^{III} in {DyCu$_3$} is best described by $M_J = \pm 13/2$. Approximating the coordination geometry of the Ln^{III} ions in {LnCu$_3$} as square antiprismatic (shape measurements relative to D_{4d} are 3.16 and 3.03 for {TbCu$_3$} and {DyCu$_3$}, respectively) allows comparison to mononuclear Ln^{III} SMMs with that geometry,[20] where it was found that the Tb^{III} ion has a maximum $M_J = \pm J = \pm 6$ ground state, and for Dy^{III} the lowest Kramers doublet is characterized by $M_J = \pm 13/2$, in good agreement with the magnetization fits for {TbCu$_3$} and {DyCu$_3$}.

Single-Molecule Magnetism. Both {TbCu$_3$} and {DyCu$_3$} display frequency-dependent (ν) slow magnetic relaxation in low-temperature ac susceptibility measurements (Figures 5 and 6), with {TbCu$_3$} showing distinct peaks in χ'' vs T, without application of a dc field. For the Arrhenius analysis ($\tau = \tau_0 \exp(\Delta E/k_B T)$) in Figure 7, ln($\tau$/s) was plotted as a function of $1/T_{\max}$, where $\tau = 1/(2\pi\nu)$ and $T_{\max}$ is the peak position from Lorentzian fits of the peaks in χ'' vs T. For {TbCu$_3$} in zero applied dc field $\Delta E/k_B = 17.3(4)$ K ($\Delta E = 12.0(3)$ cm^{-1}), and $\tau_0 = 2.2(3) \times 10^{-7}$ s (Figure 7) could be deduced from linear fits. Application of a small dc field $H_{dc} = 1.0$ kG leads to a 12% increase in the effective anisotropy barrier ($\Delta E/k_B = 19.3(1)$ K ($\Delta E = 13.4(1)$ cm^{-1})) and $\tau_0 = 1.4(1) \times 10^{-7}$ s. {DyCu$_3$}, on the other hand, shows only a small frequency dependence in zero applied dc field, while application of $H_{dc} = 1.5$ kG allows observation of distinct peaks in χ'' vs T, giving $\Delta E/k_B = 16.2(4)$ K ($\Delta E = 11.2(3)$ cm^{-1}) and $\tau_0 = 1.8(3) \times 10^{-7}$ s, following the above analysis. While the magnetic ground state of {TbCu$_3$} is characterized by half-integer cluster M_{tot} states ($M_{tot} = \langle J_{tot}M_{tot}|\hat{J}_{z,tot}|J_{tot}M_{tot}\rangle/\hbar$, where $\vec{J}_{tot} = \vec{J} + \sum_{i=1}^{3}\vec{s}_i$), i.e. Kramers doublets, {DyCu$_3$} has integer cluster M_{tot} states (vide infra), leading to more effective QTM in {DyCu$_3$} that is strongly suppressed by the application of a dc field in the ac susceptibility experiment.

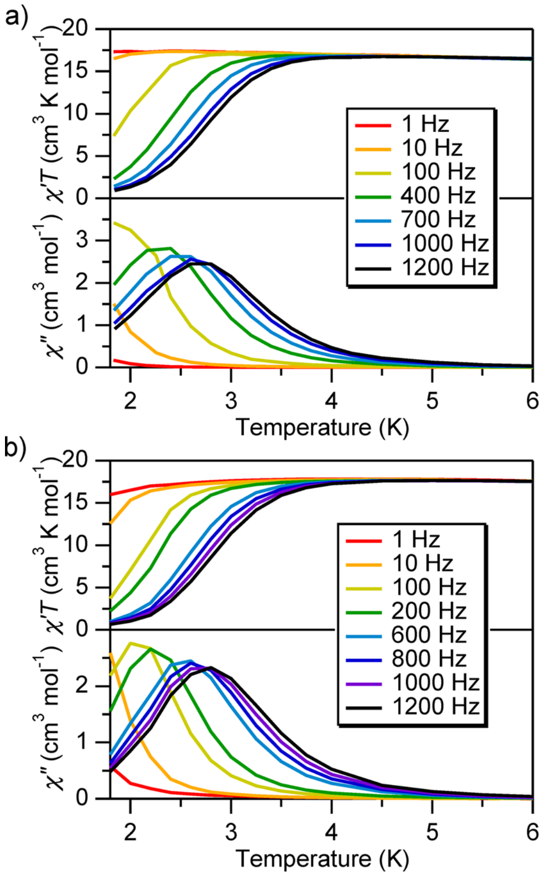

Figure 5. Magnetic ac susceptibility of {TbCu$_3$} in $H_{dc} = 0$ (a) and in $H_{dc} = 1.0$ kG (b). χ' and χ'' are the in-phase (real) and out-of-phase (imaginary) contributions, respectively.

The higher rate of QTM in {DyCu$_3$} in comparison to {TbCu$_3$} is confirmed in the low-temperature, single-crystal magnetization vs field curves shown in Figures 8 and 9. {TbCu$_3$} shows SMM-typical sweep-rate-dependent hysteresis curves with nonzero coercivity (Figure 8), and only at low enough sweep rates and high enough temperatures can the coercivity be suppressed. For {DyCu$_3$}, on the other hand, there is very little dependence of the magnetization curves on the sweep rate, and there is no coercivity at all temperatures (Figure 9), only a very small hysteresis at fields close to saturation of the magnetization ("butterfly" hysteresis). The lack of coercivity paired with the fast relaxation at $H_{dc} = 0$ and slow relaxation at $H_{dc} = 1.5$ kG are clear indications that {DyCu$_3$} is an SMM with very effective ground-state QTM, in agreement with an integer M_{tot} ground state. Application of a small dc field removes the ground-state degeneracy and thus suppresses the tunneling, thereby uncovering the thermal activation energy for spin relaxation of $\Delta E/k_B = 16.2(4)$ K.

Exchange Interactions. Inelastic neutron scattering (INS) experiments were performed on ~2 g of {TbCu$_3$} and on ~1 g of {DyCu$_3$} in the temperature range 1.4−30 K on the time-of-

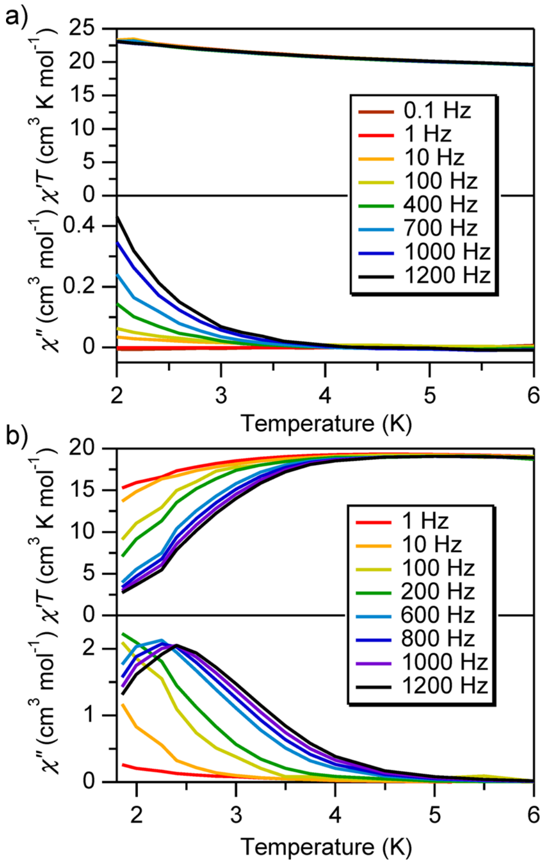

Figure 6. Magnetic ac susceptibility of {DyCu$_3$} in $H_{dc} = 0$ (a) and in $H_{dc} = 1.5$ kG (b). χ' and χ'' are the in-phase (real) and out-of-phase (imaginary) contributions, respectively.

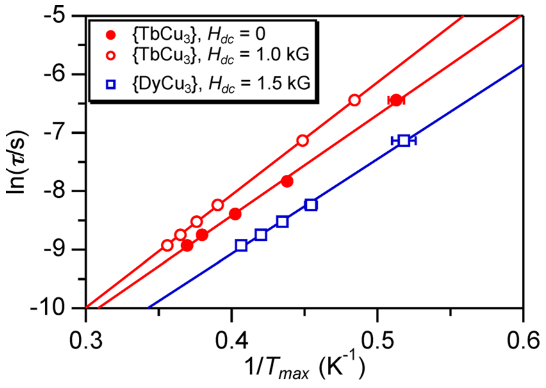

Figure 7. Arrhenius fits for {TbCu$_3$} in $H_{dc} = 0$ (red ●) and 1.0 kG (red ○) and {DyCu$_3$} in $H_{dc} = 1.5$ kG (blue □). For details, see the main text.

flight spectrometer FOCUS (Figures 10 and 11). These spectra show the scattering intensity integrated over Q ($\sim 0.4 < Q < 2.6$ Å^{-1} at $\Delta E = 0$). The Q dependence of the intensity of the INS transitions is practically featureless, apart from a small decrease with increasing Q in comparison to the rising background, and could therefore not be used for further analysis. The reason for the diffuse, structureless Q dependence and the rising background is most probably incoherent scattering due to the many hydrogen atoms in the sample.

{TbCu$_3$} was measured with two initial neutron wavelengths, 4.3 and 5.5 Å. At 4.3 Å a clear peak labeled II is observed at ~13 cm^{-1} at all three temperatures (1.4, 10, and 30 K; see Figure 10a).

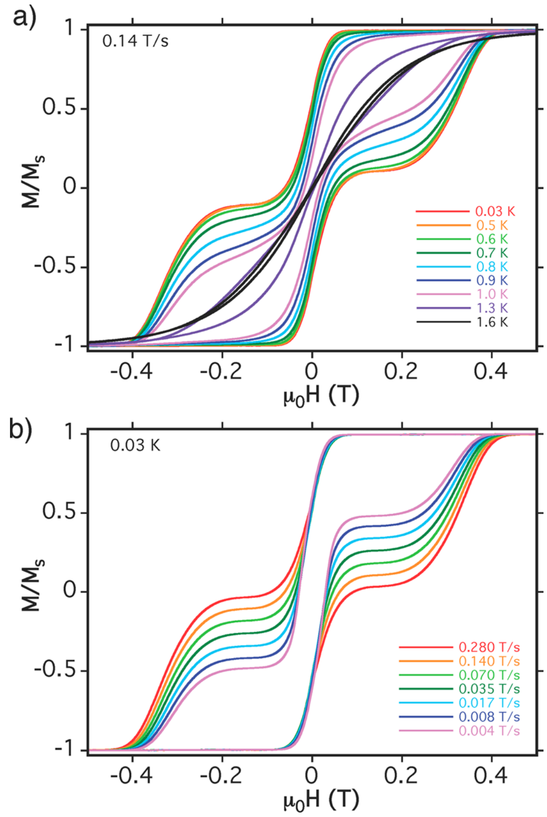

Figure 8. Single-crystal magnetization versus field hysteresis loops for {TbCu$_3$}: (a) with a constant field-sweep rate of 0.14 T/s at different temperatures between 0.03 and 1.6 K; (b) at a constant temperature of 0.03 K with different sweep rates between 0.004 and 0.280 T/s.

Additionally, a shoulder on the elastic line at ~7 cm^{-1} (I) can be seen in Figure 10a. Both features decrease in intensity with increasing temperatures and thus correspond to transitions from the ground state to different excited states. Peak II is quite broad, and the high-resolution measurement at 5.5 Å reveals that it indeed consists of multiple components. Because of the expected larger crystal-field splitting of the Tb^{III} ion, the splitting observed by these excitations has to originate from the exchange interactions between the Tb^{III} ion and the Cu^{II} ions. These interactions can be approximated to the interactions of the Tb^{III} ground M_J doublet, described as a pseudospin $S' = 1/2$, and the three Cu^{II} $s_i = 1/2$ spins using the effective Hamiltonian:

$$\mathcal{H} = -\sum_{i=1}^{3} \mathcal{J}_{ixy}(\hat{S}'_x\hat{s}_{ix} + \hat{S}'_y\hat{s}_{iy}) - \sum_{i=1}^{3} \mathcal{J}_{iz}\hat{S}'_z\hat{s}_{iz} \qquad (3)$$

i.e. eq 2 without the Zeeman terms. The three Tb^{III}−Cu^{II} exchange interactions are unrelated by symmetry, and a maximum of six parameters could be used in this axial spin Hamiltonian. Isotropic exchange interactions where $\mathcal{J}_{ixy} = \mathcal{J}_{iz}$ are unreasonable in such an effective model, as the anisotropy of the lanthanide ions due to their crystal-field splitting is absorbed into the effective exchange parameters (also an isotropic model yields two transitions with an energy ratio of 4:1, incompatible with the data). Six parameters is clearly too many for the number of observed peaks, and in a first approximation the same parameters $\mathcal{J}_{xy}$ and $\mathcal{J}_z$ were used to describe all three interactions. The dotted line in Figure 10a depicts the calculated spectrum at 1.4 K for $\mathcal{J}_{xy} = 16.6(2)$ and $\mathcal{J}_z = 26.7(2)$ cm^{-1}. This simple model fails to capture the small splitting of peak II but

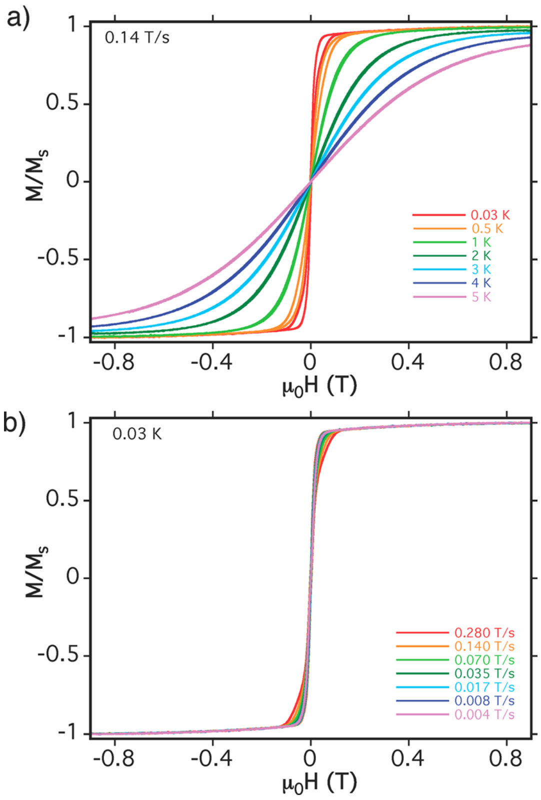

Figure 9. Single-crystal magnetization versus field hysteresis loops for $\{DyCu_3\}$: (a) with a constant field-sweep rate of 0.14 T/s at different temperatures between 0.03 and 5 K; (b) at a constant temperature of 0.03 K with different sweep rates between 0.004 and 0.280 T/s.

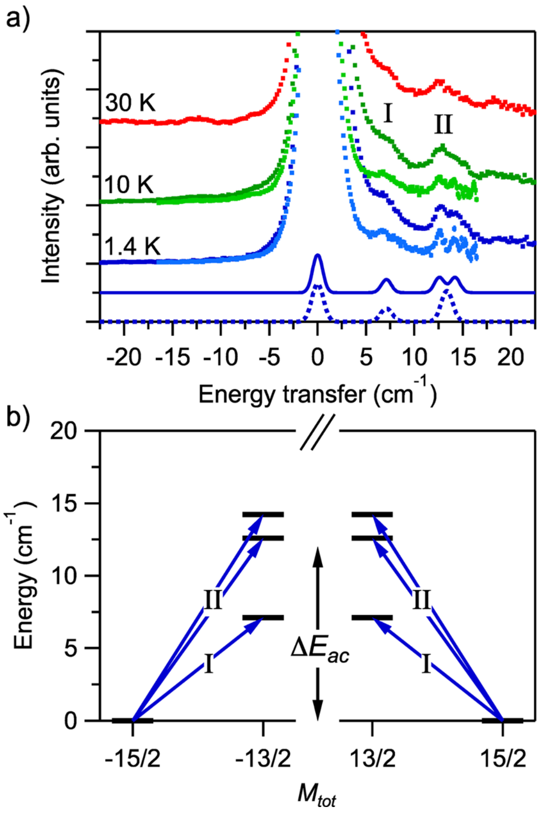

Figure 10. (a) INS spectra of $\{TbCu_3\}$ at 1.4, 10, and 30 K with 4.3 Å and at 1.4 and 10 K with 5.5 Å (light blue and light green), integrated over all angles: (dotted line) calculated spectrum at 1.4 K with J_{xy} = 16.6(2) cm^{-1} and J_z = 26.7(2) cm^{-1}; (solid line) calculated spectrum at 1.4 K with J_{1xy} = 16.6(2) cm^{-1}, J_{2xy} = 14.8(1) cm^{-1}, J_{3xy} = 18.4(1) cm^{-1}, J_{1z} = 26.7(6) cm^{-1}, J_{2z} = 23.8(5) cm^{-1}, and J_{3z} = 29.6(6) cm^{-1} (parameter restrictions as described in the main text). (b) Energy level diagram based on effective exchange interactions. Blue arrows denote INS transitions I and II. ΔE_{ac} = 12.0 cm^{-1}, the energy barrier determined by ac susceptibility (see Figure 7).

otherwise yields a reasonable description of the experimental spectrum (and these parameters were therefore used for the magnetization fits; vide supra). A calculated spectrum where peak II is split into multiple components can be obtained by varying the parameters for the three different $Tb^{III}-Cu_i^{II}$ exchange interactions. Peak II only splits into two components, even for six completely different exchange interaction parameters, and peak I does not split at all. Therefore, we limited the number of parameters by assuming a constant ratio $\mathcal{J}_{iz}/\mathcal{J}_{ixy}$ and a symmetric variation of the three exchange parameters: $\mathcal{J}_{1xy} - \mathcal{J}_{2xy} = \mathcal{J}_{3xy} - \mathcal{J}_{1xy}$. The best agreement with the measured spectra was achieved for $\mathcal{J}_{1xy}$ = 16.6(2) cm^{-1}, J_{2xy} = 14.8(1) cm^{-1}, J_{3xy} = 18.4(1) cm^{-1}, and $\mathcal{J}_{iz}/\mathcal{J}_{ixy}$ = 1.61(3) (solid line in Figure 10a).[24] Substituting the real quantum number $M_J = \pm 6$ for S' allows construction of the cluster wave functions, best described with the total magnetic quantum number $M_{tot} = \langle J_{tot}M_{tot}|\hat{J}_{z,tot}|J_{tot}M_{tot}\rangle/\hbar$. The ground state of $\{TbCu_3\}$ has M_{tot} = ±15/2, and the INS excitations are to the ±13/2 states, in agreement with the INS selection rules ($\Delta M_{tot} = 0, \pm 1$), shown in Figure 10b. Due to the ferromagnetic exchange interactions, the cluster ground state ±15/2 arises from a parallel alignment of the Tb^{III} moment and the Cu^{II} spins, and the INS excitations are Cu^{II} spin flips.

For $\{DyCu_3\}$ a thinner sample had to be used due to the large neutron absorption cross section of Dy, and it was thus not possible to measure at a wavelength of 5.5 Å, where the neutron flux is lower and the neutron absorption of the sample higher. The INS spectra of $\{DyCu_3\}$ recorded with a wavelength of 4.3 Å are depicted in Figure 11a. At 1.4 K clear peaks at ~10 and ~14 cm^{-1} are observed, which decrease in intensity with increasing temperature. These excitations are also expected to arise from the exchange interactions between the central Dy^{III} ion and the three Cu^{II} spins, as the crystal-field splitting of the Dy^{III} ion is expected to be larger than the measured energy range. Calculating the spectra for the best fit of peak position to the calculated energies yields the dotted line in Figure 11a for $\mathcal{J}_{xy}$ = 13.1(1) and $\mathcal{J}_z$ = 27.7(1) cm^{-1}. However, in $\{DyCu_3\}$ as in $\{TbCu_3\}$, peak II is broadened and may be best assumed to consist of multiple components. The same analysis as for $\{TbCu_3\}$ yields the parameters $\mathcal{J}_{1xy}$ = 12.5(2) cm^{-1}, $\mathcal{J}_{2xy}$ = 11.1(1) cm^{-1}, $\mathcal{J}_{3xy}$ = 13.9(1) cm^{-1}, and $\mathcal{J}_{iz}/\mathcal{J}_{ixy}$ = 2.20(5) for $\{DyCu_3\}$ and the solid line in Figure 11a. The low-energy spectrum as a function of the total magnetic quantum number M_{tot} is visualized in Figure 11b. The ground state can be described as M_{tot} = ±8 with excitations to states with ±7. As in $\{TbCu_3\}$, the observed INS excitations in $\{DyCu_3\}$ correspond to Cu^{II} spin flips.

The energies of the fundamental excitations in the $\{TbCu_3\}$ and $\{DyCu_3\}$ SMMs are comparable to the energy barriers found in the ac susceptibility, as is shown in Figures 10b and 11b. Therefore, it is safe to assume that the thermal relaxation goes via these excited states, which, as noted above, correspond to Cu^{II} spin flips.

In order to compare the values of the exchange interactions to the exchange interactions in e.g. $\{GdCu_3\}$, conversion into

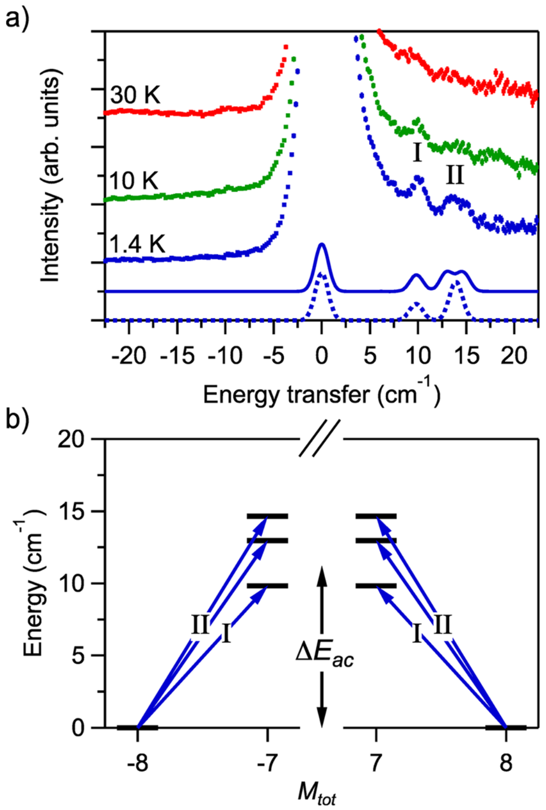

Figure 11. (a) INS spectra of {$DyCu_3$} at 1.4, 10, and 30 K with 4.3 Å, integrated over all angles: (dotted line) calculated spectrum at 1.4 K with J_{xy} = 13.1(1) cm^{-1} and J_z = 27.7(1) cm^{-1}; (solid line) calculated spectrum at 1.4 K with J_{1xy} = 12.5(2) cm^{-1}, J_{2xy} = 11.1(1) cm^{-1}, J_{3xy} = 13.9(1) cm^{-1}, J_{1z} = 27.5(8) cm^{-1}, J_{2z} = 24.4(6) cm^{-1}, and J_{3z} = 30.6(7) cm^{-1} (parameter restrictions as described in the main text). (b) Energy level diagram based on effective exchange interactions. Blue arrows denote the INS transitions I and II. ΔE_{ac} = 11.2 cm^{-1}, the energy barrier determined by ac susceptibility (see Figure 7).

Table 2. Tb⋯Cu and Dy⋯Cu Exchange Interactions

formula[a]	$\mathcal{J}_{Ln-Cu}$ (cm^{-1})	r_{Ln-Cu} (Å)	$\Delta E/k_B$ (K)	ref
{$TbCu_3$}	2.2(7)	3.2818(7), 3.2853(6), 3.2519(7)	17.3(4)	this work
{$DyCu_3$}	2.1(7)	3.2788(9), 3.2847(8), 3.2422(7)	16.2(4)[b]	this work
{TbCu}	2.1	3.4739(4)	16.6(5)[c]	7b
{Tb_2Cu_2}	2.83/0.64	3.411(2)/5.600(3)	21	10a/7a
{$TbCu_3$}	3.02	3.5989(5), 3.5988(6), 3.5709(7)	19.5(5)	7d
{TbCu}	≥2.3	3.5177(18)	42.3(4)[c]	25
{DyCu}	1.132(7)	3.510(4)	11.5(10)[c]	25
{$TbCu_2$}	1.58(4)	3.363(1), 3.660(1)	14.2(5)	26
{$DyCu_2$}	0.626(7)	3.6580(9), 3.6352(9)	N/A	26

[a] Metal ions only; for the complete structure see the references. [b] H_{dc} = 1.5 kG. [c] H_{dc} = 1 kG.

microscopic parameters is required. According to Dreiser et al.[10b] and similar to the relation between g_J and g_z, the effective axial parameter $\mathcal{J}_z$ can be expressed as $\mathcal{J}_z = 2|M_J|\mathcal{J}$. For {$TbCu_3$} with a Tb^{III} ground state $M_J = \pm 6$ and a $\mathcal{J}_z$ value of 26.7(2) cm^{-1}, the microscopic exchange interaction parameter $\mathcal{J}$ = 2.2(7) cm^{-1} is deduced. For {$DyCu_3$} $\mathcal{J}_z$ is 27.7(1) cm^{-1} and the ground state M_J of Dy^{III} is ±13/2, resulting in a microscopic $\mathcal{J}$ = 2.1(7) cm^{-1}. As can be expected, the microscopic exchange interactions between Ln^{III} and Cu^{II} ions are not too different between {$TbCu_3$} and {$DyCu_3$} and are also quite close to the value for {$GdCu_3$}, $\mathcal{J}$ = 2.9(3) cm^{-1}. These values are also similar to values found in other molecular Tb^{III}−Cu^{II} and Dy^{III}−Cu^{II} compounds,[7b,d,10a,25,26] which seem generally in the range ~0.5−3 cm^{-1} (see Table 2), depending on the distance and exact bridging geometry. The nonzero $\mathcal{J}_{xy}$ components in the effective calculations indicate that the Ln^{III} ground states are not pure M_J states and that they are more correctly described as linear combinations of wave functions with different M_J values. Our data set does not yield such details, but we justifiably presume that we used the dominant M_J contribution to the Ln^{III} ground state wave functions in our model.

■ CONCLUSIONS

In summary, we have presented two new 3d−4f SMMs, {$TbCu_3$} and {$DyCu_3$}, assembled using a step-by-step approach and provided three more examples with ferromagnetic Ln^{III}−Cu^{II} exchange interactions. Despite the somewhat similar barriers for the two SMMs (for {$TbCu_3$} in zero applied dc field $\Delta E/k_B$ = 17.3(4) K; for {$DyCu_3$} in 1.5 kG applied dc field $\Delta E/k_B$ = 16.2(4) K), strikingly different ac susceptibility and magnetic hysteresis curves are observed. The main reason for these differences lies in the different ground states, M_{tot} being a half-integer for {$TbCu_3$} and M_{tot} an integer for {$DyCu_3$}, and the associated more efficient ground state quantum tunneling of the magnetization (QTM) in {$DyCu_3$}. This highlights how the often strong QTM associated with lanthanide ions can be modulated by using 3d−4f exchange interactions. For {$TbCu_3$} and {$DyCu_3$}, the ferromagnetic exchange interactions between the central Ln^{III} ion and the three Cu^{II} ions could be accurately measured by inelastic neutron scattering (INS) spectroscopy and modeled effectively. The excitations observed by INS correspond to flipping of Cu^{II} spins and appear at energies similar to the thermodynamic barrier for relaxation of the magnetization, ~15−20 K, which we determined using ac magnetic susceptibility measurements. The Cu^{II} spin flips and hence the 3d−4f exchange interactions are thus at the origin of the SMM behavior in these exchange-coupled systems, where Cu^{II} spins coupled to the highly anisotropic Ln^{III} ion form an anisotropic cluster ground state with large M_{tot}, which can relax from one orientation to the other via Cu^{II} spin flips. This suggests that controlling and increasing the d−f exchange is essential in order to increase the blocking temperature of d−f SMMs and that, to be effective, this has to be done alongside careful control over the position of each magnetic center within the complex.

■ ASSOCIATED CONTENT

Ⓢ Supporting Information

Figures, a table, and CIF files giving crystallographic data and IR spectra for [$Cu_2(H_3edte)_2$][NO_3]$_2$, {$GdCu_3$}, {$TbCu_3$}, and {$DyCu_3$}, shape measurements of {$LnCu_3$}, diffuse reflectance spectra, and contour plots. This material is available free of charge via the Internet at http://pubs.acs.org.

■ AUTHOR INFORMATION

Corresponding Authors

*E-mail for S.T.O.: stefan.ochsenbein@psi.ch.
*E-mail for M.M.: Mark.Murrie@glasgow.ac.uk.

Notes

The authors declare no competing financial interest.

■ ACKNOWLEDGMENTS

The research leading to these results has received funding from the UK Engineering and Physical Sciences Research Council (grant ref EP/I027203/1) and the European Community's Seventh Framework Programme (FP7/2007-2013) under grant agreement No. 290605 (PSI-FELLOW/COFUND). This work is partially based on experiments performed at the Swiss spallation neutron source SINQ, Paul Scherrer Institute, Villigen, Switzerland.

■ REFERENCES

(1) (a) Ganzhorn, M.; Klyatskaya, S.; Ruben, M.; Wernsdorfer, W. *Nat. Nanotechnol.* **2013**, *8*, 165. (b) Vincent, R.; Klyatskaya, S.; Ruben, M.; Wernsdorfer, W.; Balestro, F. *Nature* **2012**, *488*, 357.

(2) Milios, C. J.; Inglis, R.; Vinslava, A.; Bagai, R.; Wernsdorfer, W.; Parsons, S.; Perlepes, S. P.; Christou, G.; Brechin, E. K. *J. Am. Chem. Soc.* **2007**, *129*, 12505.

(3) (a) Sessoli, R.; Powell, A. K. *Coord. Chem. Rev.* **2009**, *253*, 2328. (b) Woodruff, D. N.; Winpenny, R. E. P.; Layfield, R. A. *Chem. Rev.* **2013**, *113*, 5110. (c) Zhang, P.; Guo, Y. N.; Tang, J. K. *Coord. Chem. Rev.* **2013**, *257*, 1728.

(4) Rinehart, J. D.; Long, J. R. *Chem. Sci.* **2011**, *2*, 2078.

(5) Benelli, C.; Gatteschi, D. *Chem. Rev.* **2002**, *102*, 2369.

(6) Blagg, R. J.; Ungur, L.; Tuna, F.; Speak, J.; Comar, P.; Collison, D.; Wernsdorfer, W.; McInnes, E. J. L.; Chibotaru, L. F.; Winpenny, R. E. P. *Nat. Chem.* **2013**, *5*, 673.

(7) (a) Osa, S.; Kido, T.; Matsumoto, N.; Re, N.; Pochaba, A.; Mrozinski, J. *J. Am. Chem. Soc.* **2004**, *126*, 420. (b) Kajiwara, T.; Nakano, M.; Takaishi, S.; Yamashita, M. *Inorg. Chem.* **2008**, *47*, 8604. (c) Feltham, H. L. C.; Clerac, R.; Ungur, L.; Vieru, V.; Chibotaru, L. F.; Powell, A. K.; Brooker, S. *Inorg. Chem.* **2012**, *51*, 10603. (d) Feltham, H. L. C.; Clerac, R.; Ungur, L.; Chibotaru, L. F.; Powell, A. K.; Brooker, S. *Inorg. Chem.* **2013**, *52*, 3236−3240.

(8) Furrer, A. *Int. J. Mod. Phys. B* **2010**, *24*, 3653.

(9) (a) Dönni, A.; Furrer, A.; Blank, H.; Heidemann, A.; Güdel, H. U. *J. Phys. Colloques* **1988**, *49*, C8-1513. (b) Furrer, A.; Güdel, H. U.; Blank, H.; Heidemann, A. *Phys. Rev. Lett.* **1989**, *62*, 210. (c) Güdel, H. U.; Furrer, A.; Blank, H. *Inorg. Chem.* **1990**, *29*, 4081. (d) Furrer, A.; Güdel, H. U.; Krausz, E. R.; Blank, H. *Phys. Rev. Lett.* **1990**, *64*, 68. (e) Aebersold, M. A.; Güdel, H. U.; Furrer, A.; Blank, H. *Inorg. Chem.* **1994**, *33*, 1133.

(10) (a) Klokishner, S. I.; Ostrovsky, S. M.; Reu, O. S.; Palii, A. V.; Tregenna-Piggott, P. L. W.; Brock-Nannestad, T.; Bendix, J.; Mutka, H. *J. Phys. Chem. C* **2009**, *113*, 8573. (b) Dreiser, J.; Pedersen, K. S.; Piamonteze, C.; Rusponi, S.; Salman, Z.; Ali, M. E.; Schau-Magnussen, M.; Thuesen, C. A.; Piligkos, S.; Weihe, H.; Mutka, H.; Waldmann, O.; Oppeneer, P.; Bendix, J.; Nolting, F.; Brune, H. *Chem. Sci.* **2012**, *3*, 1024. (c) Reu, O.; Palii, A.; Ostrovsky, S.; Wallace, W.; Zaharko, O.; Chandrasekhar, V.; Clerac, R.; Klokishner, S. *J. Phys. Chem. C* **2013**, *117*, 6880. (d) Kofu, M.; Yamamuro, O.; Kajiwara, T.; Yoshimura, Y.; Nakano, M.; Nakajima, K.; Ohira-Kawamura, S.; Kikuchi, T.; Inamura, Y. *Phys. Rev. B* **2013**, *88*, 064405.

(11) Sheldrick, G. M. *Acta Crystallogr., Sect. A* **2008**, *A64*, 112.

(12) Wernsdorfer, W. *Adv. Chem. Phys.* **2001**, *118*, 99.

(13) Azuah, R. T.; Kneller, L. R.; Qiu, Y. M.; Tregenna-Piggott, P. L. W.; Brown, C. M.; Copley, J. R. D.; Dimeo, R. M. *J. Res. Natl. Inst. Stand. Technol.* **2009**, *114*, 341.

(14) Milway, V. A.; Tuna, F.; Farrell, A. R.; Sharp, L. E.; Parsons, S.; Murrie, M. *Angew. Chem., Int. Ed.* **2013**, *52*, 1949.

(15) (a) Saha, A.; Thompson, M.; Abboud, K. A.; Wernsdorfer, W.; Christou, G. *Inorg. Chem.* **2011**, *50*, 10476. (b) Akhtar, M. N.; Mereacre, V.; Novitchi, G.; Tuchagues, J.-P.; Anson, C. E.; Powell, A. K. *Chem. Eur. J.* **2009**, *15*, 7278.

(16) de Sousa, A. S.; Fernandes, M. A. *Polyhedron* **2002**, *21*, 1883.

(17) Casanova, D.; Llunell, M.; Alemany, P.; Alvarez, S. *Chem. Eur. J.* **2005**, *11*, 1479.

(18) Baldoví, J. J.; Cardona-Serra, S.; Clemente-Juan, J. M.; Coronado, E.; Gaita-Ariño, A.; Palii, A. *Inorg. Chem.* **2012**, *51*, 12565.

(19) Li, D.-P.; Zhang, X.-P.; Wang, T.-W.; Ma, B.-B.; Li, C.-H.; Li, Y.-Z.; You, X.-Z. *Chem. Commun.* **2011**, *47*, 6867.

(20) (a) Ishikawa, N.; Sugita, M.; Ishikawa, T.; Koshihara, S.; Kaizu, Y. *J. Phys. Chem. B* **2004**, *108*, 11265. (b) AlDamen, M. A.; Clemente-Juan, J. M.; Coronado, E.; Martí-Gastaldo, C.; Gaita-Ariño, A. *J. Am. Chem. Soc.* **2008**, *130*, 8874.

(21) Moggach, S. A.; Galloway, K. W.; Lennie, A. R.; Parois, P.; Rowantree, N.; Brechin, E. K.; Warren, J. E.; Murrie, M.; Parsons, S. *CrystEngComm* **2009**, *11*, 2601.

(22) Tregenna-Piggott, P. L. W. *MagProp (part of the NIST DAVE software suite), version 2.0*; 2008; http://www.ncnr.nist.gov/dave.

(23) (a) Bencini, A.; Gatteschi, D. *EPR of Exchange Coupled Systems.* Springer: Berlin, 1990. (b) Sorace, L.; Benelli, C.; Gatteschi, D. *Chem. Soc. Rev.* **2011**, *40*, 3092−3104.

(24) Borras-Almenar, J. J.; Clemente-Juan, J. M.; Coronado, E.; Tsukerblat, B. S. *J. Comput. Chem.* **2001**, *22*, 985−991.

(25) Ishida, T.; Watanabe, R.; Fujiwara, K.; Okazawa, A.; Kojima, N.; Tanaka, G.; Yoshii, S.; Nojiri, H. *Dalton Trans.* **2012**, *41*, 13609.

(26) Shimada, T.; Okazawa, A.; Kojima, N.; Yoshii, S.; Nojiri, H.; Ishida, T. *Inorg. Chem.* **2011**, *50*, 10555−10557.

■ NOTE ADDED AFTER ASAP PUBLICATION

Due to a production error, this paper was published on the Web on August 7, 2014, with errors in equation 2. The corrected version was reposted on August 11, 2014.